Science Robotics

robotics.sciencemag.org/cgi/content/full/2/3/eaal2505/DC1

# Supplementary Materials for

## A biomimetic robotic platform to study flight specializations of bats

Alireza Ramezani, Soon-Jo Chung,* Seth Hutchinson

*Corresponding author. Email: sjchung@caltech.edu

Published 1 February 2017, *Sci. Robot.* **2**, eaal2505 (2017)
DOI: 10.1126/scirobotics.aal2505

**The PDF file includes:**



**Other Supplementary Material for this manuscript includes the following:**
(available at robotics.sciencemag.org/cgi/content/full/2/3/eaal2505/DC1)

Movie S1 (.mp4 format). Membrane.
Movie S2 (.mp4 format). Articulated skeleton.
Movie S3 (.mp4 format). Straight flights.
Movie S4 (.mp4 format). Swoop maneuver.
Movie S5 (.mp4 format). Banking turn maneuver.

## Supplementary Text

## Wing Kinematics

Each armwing (shown in Fig. 2B) can actively produce three biological DoFs by activating a single actuator. To make this happen, we took a three-step prototyping process (34). First, we developed a fully actuated armwing. Then, a 1-DoF constrained mechanism was developed that had a rotary input. We replaced the rotary input in the 1-DoF mechanism with a linear input resulting in the current design.

The first prototype was a three-link mechanism with independent actuators at each joint that could move each link relative to another link. Regulating the position and orientation of the end-effector in this three-link mechanism implies direct control of the three revolute joints, which requires extra electronics (sensors, motor drivers); thereby, causing extra payload. We removed all of the actuators and introduced three more rigid links (constraints), which led to a six-bar linkage known as Watt mechanism (please, see (34)). This mechanism is a 1-DoF mechanism that requires only one actuator. To activate this mechanism with a linear actuator we modified the Watt mechanism. In this mechanism, the linear motion of the radius link (point $p_2$ in Fig. 2B) at the shoulder moves humerus link relative to the shoulder joint (point $p_0$) and results in the flexion and extension of the elbow. Other movements are described in the main manuscript.

Now, to mathematically describe the kinematics of the armwing mechanism, we assume that all of the links in the wing mechanism are rigid and that all of the joints are 1-DoF revolute joints. Thereby, each forelimb mechanism is uniquely defined with only one configuration variable. In other words, by knowing the linear position of the spindle drive, which is shown in Fig. 2B, the configuration of the forelimbs is determined (34).

In this model development, the angles are measured as following. The retraction-protraction is measured with respect to the body x-axis (shown in Fig. 2A); radial flexion-extension is measured with respect to the humeral link; carpal abduction-adduction is measured relative to the radial link. The angles read positive when rotating counterclockwise. The position of each point on the forelimb mechanism is given by

$$\begin{cases} [p_i]_{\mathcal{F}_\mathrm{s}} = [p_2]_{\mathcal{F}_\mathrm{s}} + \mathcal{R}(q_\mathrm{RP})[p_i]_{\mathcal{F}_\mathrm{r}}, \quad i \in \{1,2,3\} \\ [p_i]_{\mathcal{F}_\mathrm{s}} = [p_1]_{\mathcal{F}_\mathrm{s}} + \mathcal{R}(q_\mathrm{RP} + q_\mathrm{FE})[p_i]_{\mathcal{F}_\mathrm{r}}, \quad i \in \{0,5\} \\ [p_i]_{\mathcal{F}_\mathrm{s}} = [p_3]_{\mathcal{F}_\mathrm{s}} + \mathcal{R}(q_\mathrm{RP} + q_\mathrm{FE} + q_\mathrm{AA})[p_i]_{\mathcal{F}_\mathrm{c}}, \quad i \in \{4,6,7,8\} \\ [p_2]_{\mathcal{F}_\mathrm{s}} = (0, y_\mathrm{spindle}(t), 0)' \end{cases} \tag{1}$$

where $(')$ is the matrix transpose operator and $\mathcal{F}_\mathrm{s}$, $\mathcal{F}_\mathrm{h}$, $\mathcal{F}_\mathrm{r}$, and $\mathcal{F}_\mathrm{c}$ are the body coordinate frames attached to the shoulder, humerus, radius and carpus (shown in Fig. 2B). In Eq. 1, $\mathcal{R}$ is the rotation matrix; $[p_i]_j$ is the position of i-th point in the

body coordinate frame j. Now, the sliding constraint, which is introduced by the linear motion of the spindle drive, is incorporated into the wing kinematic equations as follows.

$$\textbf{const}: \mathbf{G}(q_{\mathrm{RP}}, q_{\mathrm{FE}}, q_{\mathrm{AA}}, y_{\mathrm{spindle}}) = [p_2]_{\mathcal{F}_\mathrm{s}} - [p_1]_{\mathcal{F}_\mathrm{s}} - \mathcal{R}(q_{\mathrm{RP}} + q_{\mathrm{FE}})[p_2]_{\mathcal{F}_\mathrm{h}}. \qquad 2$$

Solving the nonlinear equations given by Eq. 1 subject to the constraint Eq. 2 results in the trajectories of the forelimb links and joints.

## Actuation

**Armwing:** Each wing actuator, which is composed of a planetary gearhead, a spindle drive, and a 6 mm DC gearmotor (model 206-102 from Precision Micro Drives), produces the required linear motion. The planetary gearhead increases the output torque, and the threaded rod, which is attached to the gearhead on one side and screwed to the shoulder on the other side, pushes or pulls the shoulder depending on the direction of rotation of the spindle.

At the nominal operating condition, the DC motor produces angular velocity of 3400 rad/s, which is geared down to 136 rad/s utilizing the planetary gearhead. The resulting linear motion of the spindle measures 10 cm/s, which yields fast mediolateral movements of the wings.

A magnetic Hall effect sensor at the elbow measures the relative movements of the humeral link with respect to the radial link. This mechanism has 1-DoF flapping motion around the shoulder bar. The flapping motion is realized utilizing a crank-shaft mechanism. A brushless DC motor, which is employed after it is geared down using a combination of spur compound gears embedded inside the fuselage, drives a crank where an eccentrically attached flapping rod translates the rotary motion to the push-pulls of the contact joint on the wing. The flapping mechanism synchronously produces flapping motions in the right and left wings.

**Legs (hindlimbs):** A lead-screw drive, similar to the forelimb spindle drive, yields linear movements of the actuation bar as a threaded rod travels inside a threaded hole in the actuation bar. When the actuation bar is at its far ends, the legs measure dorsoventral angles 30 (degree) relative to the body. A Hall effect encoder reads the relative angle of the leg with respect to the body.

## Generalized Forces

The generalized forces on the right hand side of

$$\mathcal{M}(\boldsymbol{q})\ddot{\boldsymbol{q}} + \mathcal{C}(\boldsymbol{q}, \dot{\boldsymbol{q}})\dot{\boldsymbol{q}} + \mathcal{G}(\boldsymbol{q}) = \mathcal{Q}_{gen} \qquad 3$$

are the resultant of the joint constraint torques acting on the actuated coordinates $\boldsymbol{q}_{\mathrm{act}}$ and the wings aerodynamic forces. Employing the principle of virtual work, the

generalized constraint torques are given by

$$\mathcal{Q}_{\text{cons}} = \left(\frac{\partial \boldsymbol{q}_{\text{act}}}{\partial \boldsymbol{q}}\right)' \boldsymbol{\lambda} \tag{4}$$

where $\boldsymbol{\lambda} \in \mathbb{R}^5$ denotes the constraint torques. As for the aerodynamic forces, the aerodynamic model (47) is applied to the wings utilizing blade theory. The proposed aerodynamic model is in the form of an Ordinary Differential Equation (ODE) and two algebraic equations. The ODE, which is given below, estimates the position of the separation point for unsteady flow conditions (47)

$$\tau_1 \dot{v} + v = v_0(\alpha - \tau_2 \dot{\alpha}) \tag{5}$$

where $v$ is the position of the separation point and $\tau_1$ is the relaxation time constant. The constant term $\tau_2$ denotes the time delay effects due to the flow, and $v_0$ is the position of the separation point at the steady-state condition; $\alpha$ is the angle of attack and is evaluated as following

$$\alpha = \cos^{-1}\left((\boldsymbol{e}_t)' \frac{\left(\frac{\partial \boldsymbol{p}_{cp}}{\partial \boldsymbol{q}}\dot{\boldsymbol{q}}\right)}{\left\|\left(\frac{\partial \boldsymbol{p}_{cp}}{\partial \boldsymbol{q}}\dot{\boldsymbol{q}}\right)\right\|_2}\right). \tag{6}$$

In Eq. 6, $\left(\frac{\partial \boldsymbol{p}_{cp}}{\partial \boldsymbol{q}}\dot{\boldsymbol{q}}\right)$ denotes the velocity of CoP and $\boldsymbol{e}_t$ is a chordwise unit vector. The coefficient of lift is given by (47)

$$C_l = \frac{\pi}{2}\sin\alpha \times \left(1 + v + 2\sqrt{v}\right), \tag{7}$$

and the quarter-chord moment is given by (47)

$$C_m = \frac{\pi}{2}\sin\alpha \times \left(1 + v + 2\sqrt{v}\right) \times \left(\frac{5 + 5v - 6\sqrt{v}}{16}\right). \tag{8}$$

The magnitude of the lift force and quarter-chord moment are given by (48)

$$\|\boldsymbol{F}_l\|_2 = 0.5\rho_{\text{air}} c C_l \left(\frac{\partial \boldsymbol{p}_{cp}}{\partial \boldsymbol{q}}\dot{\boldsymbol{q}}\right)' \left(\frac{\partial \boldsymbol{p}_{cp}}{\partial \boldsymbol{q}}\dot{\boldsymbol{q}}\right) + \frac{\pi}{4}\rho_{\text{air}} c^2 \left(\ddot{\zeta} + V_\infty \dot{\alpha} - c(x_a - 0.25)\ddot{\alpha}\right), \tag{9}$$

and

$$\begin{aligned}\|\boldsymbol{M}_m\|_2 = {} & 0.5\rho_{\text{air}} c^2 C_m \left(\frac{\partial \boldsymbol{p}_{cp}}{\partial \boldsymbol{q}}\dot{\boldsymbol{q}}\right)' \left(\frac{\partial \boldsymbol{p}_{cp}}{\partial \boldsymbol{q}}\dot{\boldsymbol{q}}\right) + \\ & \frac{\pi}{4}\rho_{\text{air}} c^2 \left(V_\infty \dot{\zeta} + \frac{c(x_a - 0.25)\ddot{\zeta}}{2} + V_\infty^2 \alpha - c^2 \left(\frac{1}{32} + (x_a - 0.25)^2\right)\ddot{\alpha}\right).\end{aligned} \tag{10}$$

In Eqs. 9 and 10, the transverse displacement of the wing due to the wing deformation ($\zeta$) is ignored. The chord length, air density, and free-stream velocity are denoted by $c$, $\rho_{\text{air}}$, and $V_\infty$, respectively. Unfortunately, there is no simple expression for the sectional drag coefficient $C_d$ (48). A drag model that incorporates dynamic stall can be found in (43).

We employed the principle of virtual work to incorporate the aerodynamic terms in the Lagrange equations. The generalized aerodynamic forces are given by

$$\mathcal{Q}_{\text{aero}} = \left(\frac{\partial \boldsymbol{p}_{cp}}{\partial \boldsymbol{q}}\right)' (\boldsymbol{F}_l + \boldsymbol{F}_d) + \left(\frac{\partial \boldsymbol{\omega}}{\partial \dot{\boldsymbol{q}}}\right)' \boldsymbol{M}_m \tag{11}$$

where $\boldsymbol{\omega}$ denotes the angular velocity vector that describes the rotation of the wings.

## Fixed-Point Design

Here, the constrained dynamics given by

$$\begin{cases} \begin{bmatrix} \ddot{\mathcal{X}} \\ \ddot{\boldsymbol{q}}_{\text{act}} \end{bmatrix} = \left( \begin{bmatrix} \mathcal{M}_{11} & \mathcal{M}_{12} \\ \mathcal{M}_{21} & \mathcal{M}_{22} \end{bmatrix} \right)^{-1} \left( - \begin{bmatrix} \mathcal{C}_{11} & \mathcal{C}_{12} \\ \mathcal{C}_{21} & \mathcal{C}_{22} \end{bmatrix} \begin{bmatrix} \dot{\mathcal{X}} \\ \dot{\boldsymbol{q}}_{\text{act}} \end{bmatrix} - \begin{bmatrix} \mathcal{G}_1 \\ \mathcal{G}_2 \end{bmatrix} + \mathcal{Q}_{\text{cons}} + \mathcal{Q}_{\text{aero}}(\boldsymbol{q}, \dot{\boldsymbol{q}}) \right) \\ \ddot{\boldsymbol{q}}_{\text{act}} = \left(\frac{\partial \boldsymbol{N}}{\partial \boldsymbol{q}_{\text{act}}}\right)^{-1} \left( -\kappa_1 \dot{\boldsymbol{N}} - \kappa_2 \boldsymbol{N} - \frac{\partial^2 \boldsymbol{N}}{\partial t^2} - \frac{\partial}{\partial \boldsymbol{q}_{\text{act}}} \left( \frac{\partial \boldsymbol{N}}{\partial \boldsymbol{q}_{\text{act}}} \dot{\boldsymbol{q}}_{\text{act}} \right) \dot{\boldsymbol{q}}_{\text{act}} \right). \end{cases} \tag{12}$$

is exposed to a gradient-based optimization problem to find feasible periodic solutions while the following conditions shape the constraints

$$0 \leq \mathcal{Q}_{\text{cons}} \leq \mathcal{Q}_{\max}, \tag{13}$$

and

$$q_{\min} \leq q_i \leq q_{\max}. \tag{14}$$

These two equations describe the physical constraints, such as the actuator torque ($\mathcal{Q}_{\text{cons}}$) and joint angle limit ($q_i$). A shooting method (46) at the core of the optimization problem converts the initial-value problem given by Eq. 12 into a two-point boundary-value problem given by

$$\begin{bmatrix} \dot{\boldsymbol{q}} \\ \ddot{\boldsymbol{q}} \end{bmatrix} = \boldsymbol{H}(t, \boldsymbol{q}, \dot{\boldsymbol{q}}, \boldsymbol{\beta}) \tag{15}$$

where $\boldsymbol{H}$ denotes the system of nonlinear equations in Eq. 12. The boundary values are

$$\begin{aligned} \boldsymbol{q}(t_f, \boldsymbol{q}_0, \dot{\boldsymbol{q}}_0) &= \boldsymbol{q}_0, \\ \dot{\boldsymbol{q}}(t_f, \boldsymbol{q}_0, \dot{\boldsymbol{q}}_0) &= \dot{\boldsymbol{q}}_0 \end{aligned} \tag{16}$$

which reflect the periodicity of solutions by emphasizing that positions and velocities at the beginning of the flapping cycle ($\boldsymbol{q}_0$,$\dot{\boldsymbol{q}}_0$) must be equal to the ones at the end. Here, $t_f$ denotes the end of each wingbeat. Since the external forces acting on the system are periodic with the known period, the initial generalized coordinates $\boldsymbol{q}_0$ and their time derivatives $\dot{\boldsymbol{q}}_0$ are the only unknown terms. The dependence of the vectors of generalized coordinates $\boldsymbol{q}$ and $\dot{\boldsymbol{q}}$ on time and the initial states is shown by

$$\begin{aligned} \boldsymbol{q} &= \boldsymbol{q}(t, \boldsymbol{q}_0, \dot{\boldsymbol{q}}_0), \\ \dot{\boldsymbol{q}} &= \dot{\boldsymbol{q}}(t, \boldsymbol{q}_0, \dot{\boldsymbol{q}}_0). \end{aligned} \tag{17}$$

The shooting method starts with initial guesses $\boldsymbol{q}_0$ and $\dot{\boldsymbol{q}}_0$. Iteratively, it updates them to find periodic fixed points. In order to obtain the corrections $\delta\boldsymbol{q}_0$ and $\delta\dot{\boldsymbol{q}}_0$ at each iteration, the periodicity conditions are first imposed on $\boldsymbol{q}$

$$\boldsymbol{q}(t_f, \boldsymbol{q}_0 + \delta\boldsymbol{q}_0, \dot{\boldsymbol{q}}_0 + \delta\dot{\boldsymbol{q}}_0) = \boldsymbol{q}_0 + \delta\boldsymbol{q}_0 \tag{18}$$

where $t_f$ is the timespan of a single wingbeat. Applying the Taylor approximation on the left hand side of Eq. 18 gives

$$\boldsymbol{q}(t_f, \boldsymbol{q}_0 + \delta\boldsymbol{q}_0, \dot{\boldsymbol{q}}_0 + \delta\dot{\boldsymbol{q}}_0) \approx \boldsymbol{q}(t_f, \boldsymbol{q}_0, \dot{\boldsymbol{q}}_0) + \frac{\partial \boldsymbol{q}(t_f, \boldsymbol{q}_0, \dot{\boldsymbol{q}}_0)}{\partial \boldsymbol{q}_0}\delta\boldsymbol{q}_0 + \frac{\partial \boldsymbol{q}(t_f, \boldsymbol{q}_0, \dot{\boldsymbol{q}}_0)}{\partial \dot{\boldsymbol{q}}_0}\delta\dot{\boldsymbol{q}}_0. \tag{19}$$

Substituting Eq. 19 in Eq. 18 gives

$$\left(\frac{\partial \boldsymbol{q}(t_f, \boldsymbol{q}_0, \dot{\boldsymbol{q}}_0)}{\partial \boldsymbol{q}_0} - \mathcal{I}\right)\delta\boldsymbol{q}_0 + \frac{\partial \boldsymbol{q}(t_f, \boldsymbol{q}_0, \dot{\boldsymbol{q}}_0)}{\partial \dot{\boldsymbol{q}}_0}\delta\dot{\boldsymbol{q}}_0 = \boldsymbol{q}_0 - \boldsymbol{q}(t_f, \boldsymbol{q}_0, \dot{\boldsymbol{q}}_0). \tag{20}$$

Taking similar steps for $\dot{\boldsymbol{q}}$, as shown in Eq. 18, Eq. 19, and Eq. 20, gives

$$\frac{\partial \dot{\boldsymbol{q}}(t_f, \boldsymbol{q}_0, \dot{\boldsymbol{q}}_0)}{\partial \boldsymbol{q}_0}\delta\boldsymbol{q}_0 + \left(\frac{\partial \dot{\boldsymbol{q}}(t_f, \boldsymbol{q}_0, \dot{\boldsymbol{q}}_0)}{\partial \dot{\boldsymbol{q}}_0} - \mathcal{I}\right)\delta\dot{\boldsymbol{q}}_0 = \dot{\boldsymbol{q}}_0 - \dot{\boldsymbol{q}}(t_f, \boldsymbol{q}_0, \dot{\boldsymbol{q}}_0). \tag{21}$$

In Eq. 20 and Eq. 21, $\mathcal{I}$ is identity matrix. Now, Eq. 20 and Eq. 21 are re-written in the form of a linear system of equations

$$\begin{bmatrix} \delta\boldsymbol{q}_0 \\ \\ \delta\dot{\boldsymbol{q}}_0 \end{bmatrix} = \begin{bmatrix} \left(\frac{\partial \boldsymbol{q}(t_f, \boldsymbol{q}_0, \dot{\boldsymbol{q}}_0)}{\partial \boldsymbol{q}_0} - \mathcal{I}\right) & \frac{\partial \boldsymbol{q}(t_f, \boldsymbol{q}_0, \dot{\boldsymbol{q}}_0)}{\partial \dot{\boldsymbol{q}}_0} \\ \\ \frac{\partial \dot{\boldsymbol{q}}(t_f, \boldsymbol{q}_0, \dot{\boldsymbol{q}}_0)}{\partial \boldsymbol{q}_0} & \left(\frac{\partial \dot{\boldsymbol{q}}(t_f, \boldsymbol{q}_0, \dot{\boldsymbol{q}}_0)}{\partial \dot{\boldsymbol{q}}_0} - \mathcal{I}\right) \end{bmatrix}^{-1} \begin{bmatrix} \boldsymbol{q}_0 - \boldsymbol{q}(t_f, \boldsymbol{q}_0, \dot{\boldsymbol{q}}_0) \\ \\ \dot{\boldsymbol{q}}_0 - \dot{\boldsymbol{q}}(t_f, \boldsymbol{q}_0, \dot{\boldsymbol{q}}_0) \end{bmatrix}. \tag{22}$$

Now, the update terms $\boldsymbol{q}_0$ and $\dot{\boldsymbol{q}}_0$ are computable.

## Notion of Stability for Periodic Orbits

Some of the the material that is presented here is a reiteration of the material in (49-59). Our closed-loop feedback synthesis for B2 is based on the notion of stability for periodic orbits.

A solution $\varphi : [t_0, \infty) \to \mathcal{U}$[1] is a periodic solution of the autonomous system

$$\dot{x} = f(x) \tag{23}$$

if for all $t \in [t_0, \infty)$

$$\varphi(t + T) = \varphi(t) \tag{24}$$

for some minimum period $T > 0$ (57). A set $\mathcal{O}$ is a periodic orbit of Eq. 23 if

$$\mathcal{O} = \{\varphi(t) | t \geq t_0\} \tag{25}$$

for some periodic solution $\varphi(t)$. An orbit is nontrivial if it contains more than one point (59).

**Notion of stability:** Lyapunov stability (49) of the periodic orbit $\mathcal{O}$ is formally stated as if there exists a neighborhood $\mathcal{V}$ of the periodic orbit $\mathcal{O}$ such that for every point $p$ in the neighborhood $\mathcal{V}$, there exists a solution $\varphi : [t_0, \infty) \to \mathcal{U}$ of the autonomous system given by Eq. 23 satisfying $\varphi(0) = p$ and

$$\text{dist}(\varphi(t), \mathcal{O}) < \epsilon \tag{26}$$

for all $t \geq 0$, where $\epsilon > 0$, and $\text{dist}(p_1, p_2)$ is the Euclidean distance. The orbit $\mathcal{O}$ is attractive if there exists an open neighborhood $\mathcal{V}$ of $\mathcal{O}$ such that for every $p \in \mathcal{V}$, there exists a solution $\varphi : [t_0, \infty) \to \mathcal{U}$ of Eq. 23 satisfying $\varphi(0) = p$ and

$$\lim_{t \to \infty} \text{dist}(\varphi(t), \mathcal{O}) = 0. \tag{27}$$

The periodic orbit $\mathcal{O}$ is asymptotically stable in the sense of Lyapunov if it is both stable and attractive. Exponentially stability of the orbit $\mathcal{O}$ is achieved if there exists a neighborhood $\mathcal{V}$ of $\mathcal{O}$ such that for every $p \in \mathcal{V}$, there exists a solution $\varphi : [0, \infty) \to \mathcal{U}$ of the autonomous system given by Eq. 23 satisfying $\varphi(0) = p$ and

$$\text{dist}(\varphi(t), \mathcal{O}) \leq N \exp(-\gamma t) \text{dist}(p, \mathcal{O}) \tag{28}$$

where $N$ and $\gamma$ are positive constants.

**Poincare Section:** A Poincare section is a smooth hypersurface $\mathcal{S}$ in $\mathcal{U}$ and it satisfy the following conditions:

- $\mathcal{S}$ is nonempty and there exists a differentiable function $H : \mathcal{U} \to \mathbb{R}$ such that

$$\mathcal{S} := \{x \in \mathcal{U} | H(x) = 0\}; \tag{29}$$

[1] $\mathcal{U}$ is a smooth embedded submanifold of $\mathbb{R}^n$.

- for every $s \in \mathcal{S}$

$$\frac{\partial H}{\partial x}(s) \neq 0. \tag{30}$$

This condition implies that the periodic orbit $\mathcal{O}$ is transversal to $\mathcal{S}$; $\mathcal{S}$ has a lower dimension than $\mathcal{U}$.

**Method of Poincare:** Any map $\boldsymbol{P} : \mathcal{S} \to \mathcal{S}$ defines a discrete dynamic system by

$$x_{k+1} = \boldsymbol{P}(x_k) \tag{31}$$

where $x_k \in \mathcal{S}$ is the state and $\boldsymbol{P}$ maps the state to the next state $x_{k+1}$. For this discrete system

$$\boldsymbol{P}(x^*) = x^* \tag{32}$$

where $x^*$ is the fixed-point of the discrete system. When starting from an initial state $x_0$, successive application of the map $\boldsymbol{P}$ generates a sequence of states that can reveal useful information about the stability of the discrete time system (46). In other words, in the method of Poincare, there is a relationship between the periodic orbits of the system (Eq. 23) and the equilibrium points of the sampled system above. This method is interesting because it establishes an equivalence between the stability properties of the periodic orbits of Eq. 23 and the equilibrium points of the discrete system Eq. 31. This equivalence is formally expressed here in form of a theorem from (59).

**Theorem:**

Assuming that the hypothesis from (56) are satisfied, then:

- *If $\mathcal{O}$ is a periodic orbit of Eq. 23 that is transversal to $\mathcal{S}$, then there exists a point $s \in \mathcal{S}$ that generates $\mathcal{O}$.*
- *$s^* \in \mathcal{S}$ is a fixed point of $\boldsymbol{P}$, if and only if $s^*$ generates a periodic orbit $\mathcal{O}(s^*)$ that is transversal to $\mathcal{S}$.*
- *$s^* \in \mathcal{S}$ is a stable equilibrium point of $x_{k+1} = \boldsymbol{P}(x_k)$, if and only if the orbit $\mathcal{O}(s^*)$ is stable.*
- *$s^* \in \mathcal{S}$ is an asymptotically stable equilibrium point of $x_{k+1} = \boldsymbol{P}(x_k)$, if and only if the orbit $\mathcal{O}(s^*)$ is asymptotically stable.*

*Moreover, if Eq. 23 is continuously differentiable, then*

- *$s^* \in \mathcal{S}$ is an exponentially stable equilibrium point of $x_{k+1} = \boldsymbol{P}(x_k)$, if and only if the orbit $\mathcal{O}(s^*)$ is exponentially stable.*

- *$s^* \in \mathcal{S}$ is an exponentially stable equilibrium point of $x_{k+1} = \boldsymbol{P}(x_k)$, if and only if the eigenvalues of $\frac{\partial \boldsymbol{P}}{\partial x}(s^*)$, which is the Jacobian liniarization of $\boldsymbol{P}$ at $s^*$, have magnitude strictly less than one.*

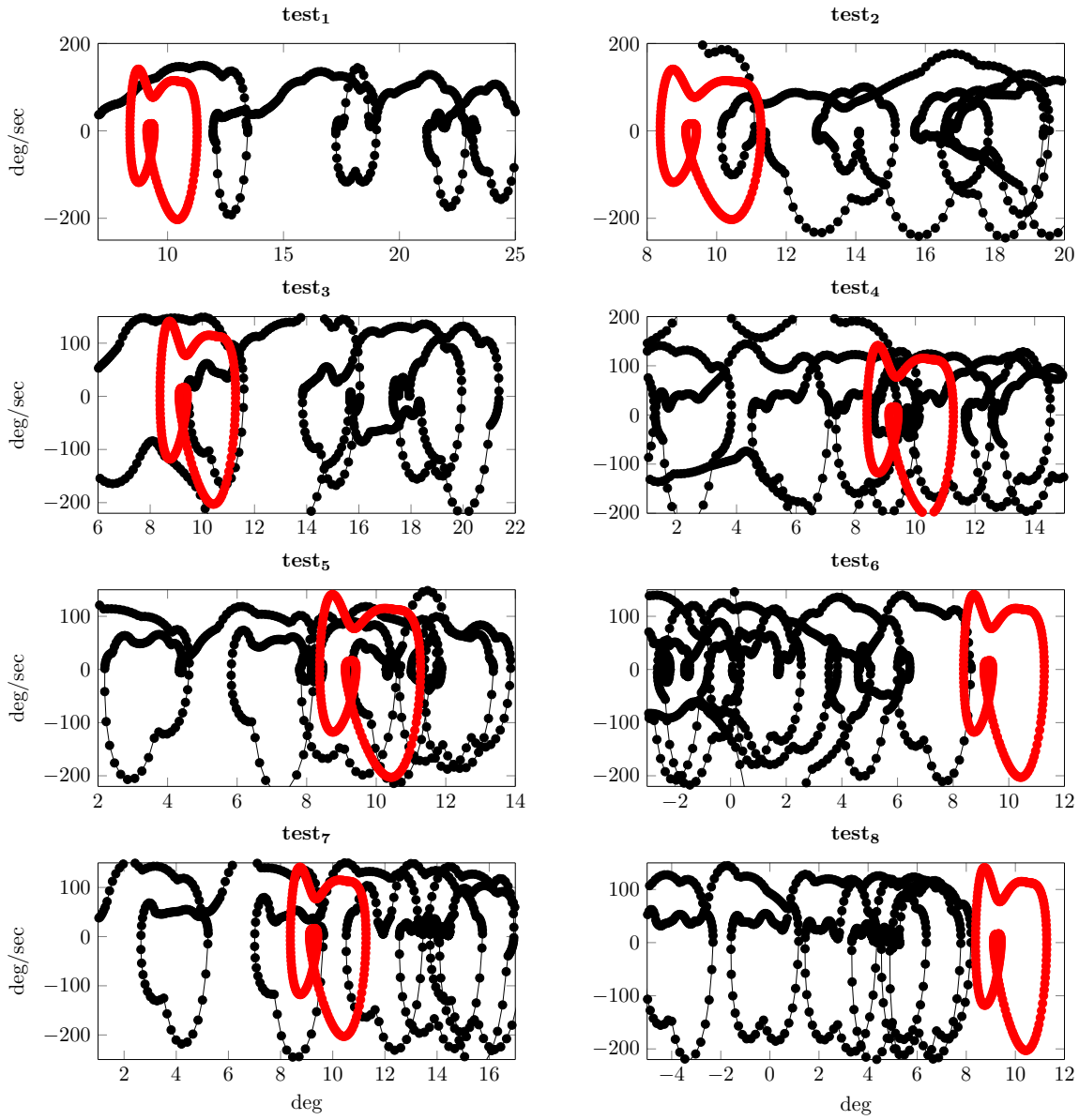


**Fig. S1. Nonlinear model verification. The simulated pitch angle phase portrait is compared with eight closed-loop flight experiments. The black and red lines are the experimental and simulation results, respectively.**

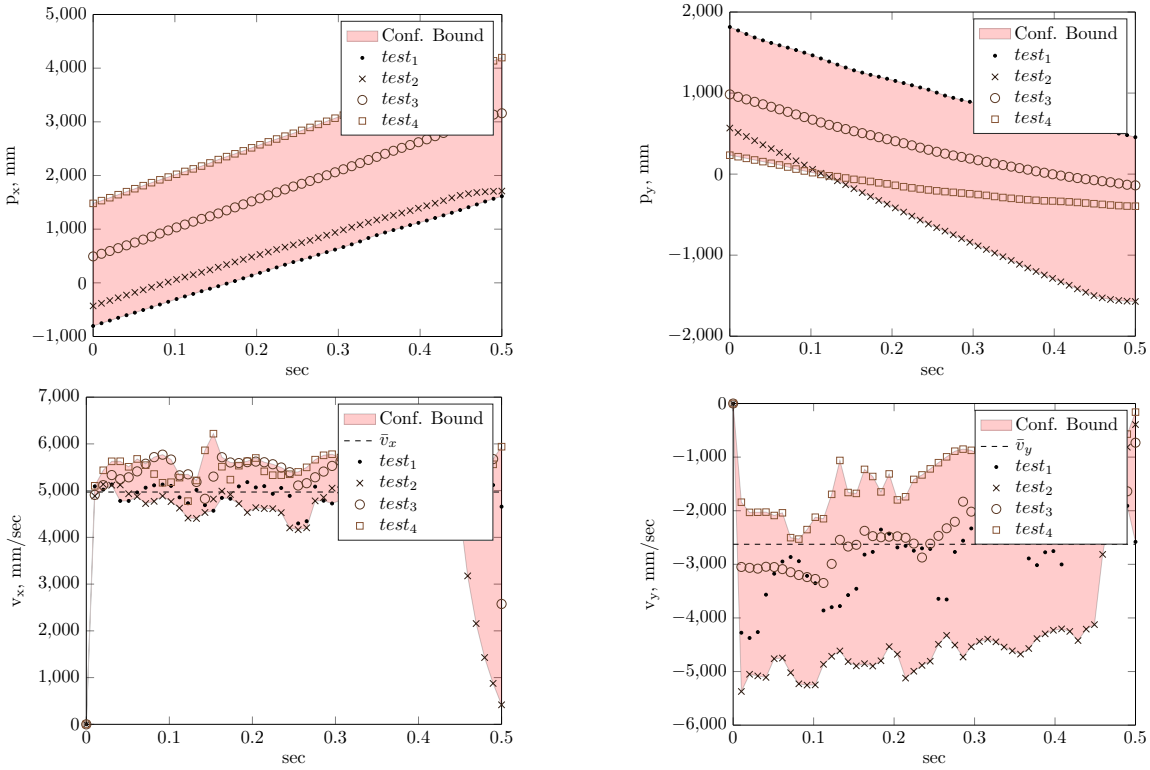


**Fig. S2. Flight speed measurements. A motion capture system was employed to measure B2's flight speed $U$ for four flight tests. The position terms $p_x$ and $p_y$ are recorded at 100 Hz. Thereafter, the time derivatives $v_x$ and $v_y$ are computed. The magnitude of the instantaneous flight speed is given by $U = \sqrt{v_x^2 + v_y^2}$.**

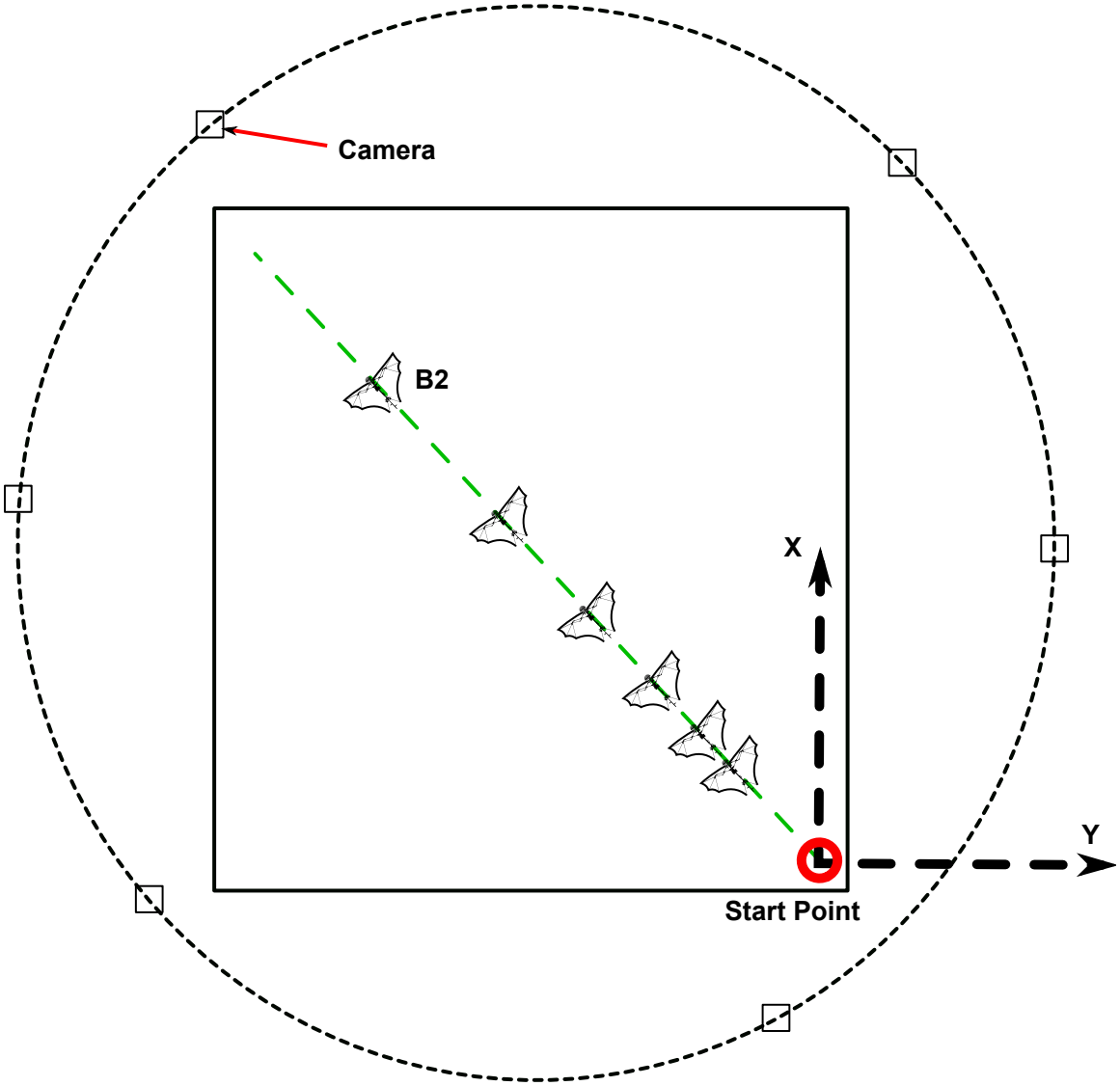


**Fig. S3. Motion capture system. The setup shown above (top view) was utilized to characterize B2's untethered flight. The robot was launched from the start point for four times and the position data recorded at 100** Hz.

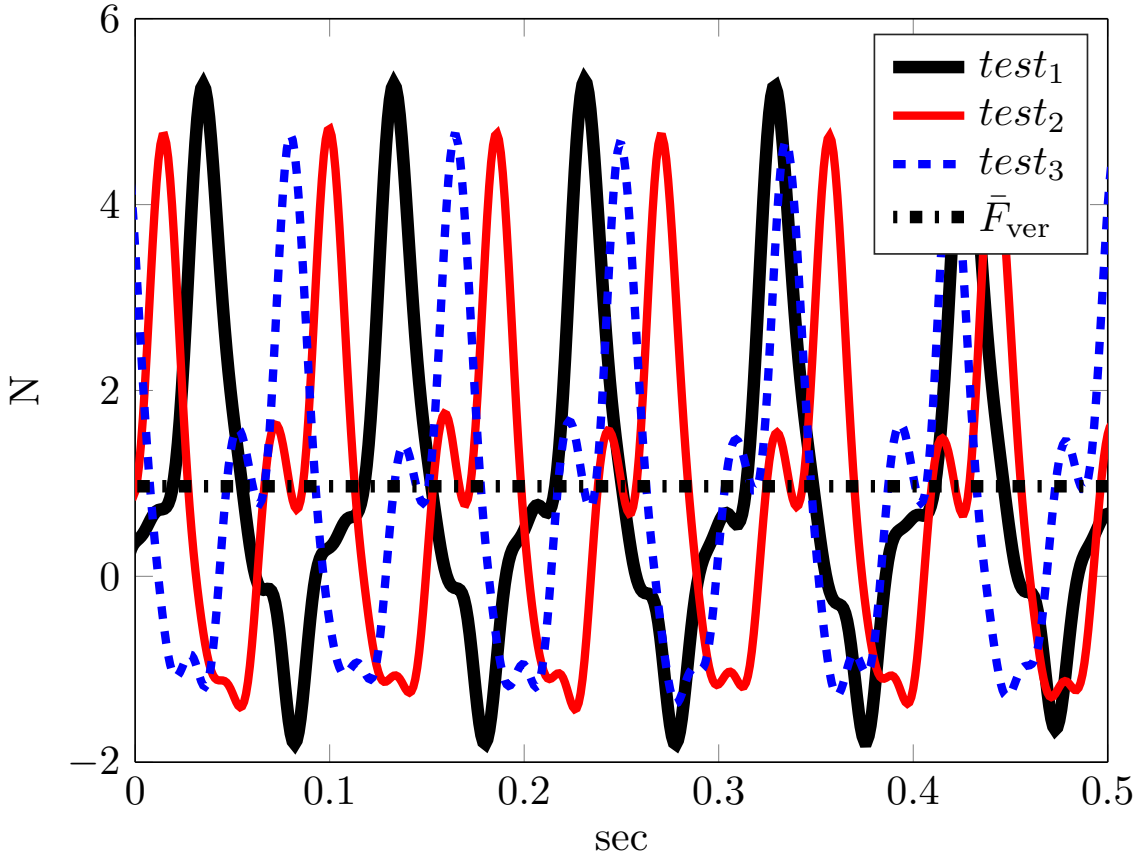


**Fig. S4. Wind tunnel measurements. For these experiments, the robot with $0$ deg pitch angle was installed inside a wind tunnel. A miniature load cell was utilized to record the produced lift force while the robot was flapping at $\approx 10$ Hz. To emulate the flight condition, the air flow inside the wind tunnel was set to $4-6$ ms$^{-1}$. These results suggest that the vertical aerodynamic force $F_{\text{ver}}$ oscillates within the range of $\approx -2$ to $5$ N. The average force $\bar{F}_{\text{ver}}$ is nearly $1$ N.**

**Table S1. B2's morphological details.**

| | B2 | *Rousettus aegyptiacus* |
|---|---|---|
| aspect ratio, - | 3.57 | 5.0 |
| flapping frequency, Hz | 10 | $\approx 10$ |
| flapping amplitude, deg | $\pm$ 27.5 | $\approx 35$ |
| mean wing span, m | 0.469 | 0.6 |
| mean wing area, m | 0.0694 | 0.072 |
| mean wing chord, m | 0.14 | 0.12 |
| total mass, kg | 0.093 | 0.16 |
| body width, m | 0.02 | 0.035 |
| humerus (arm) length, m | 0.035 | 0.038 |
| radius (forearm) length, m | 0.045 | 0.068 |
| digits (fingers) length, m | 0.14 | 0.12 |
| femur (leg) length, m | 0.1 | 0.055 |

**Movie S1**
Membrane.

**Movie S2**
Articulated Skeleton.

**Movie S3**
Straight Flights.

**Movie S4**
Swoop Maneuver.

**Movie S5**
Banking Turn Maneuver.